



Solvent mediated surface engineering of α -Fe₂O₃ nano materials: Facet sensitive energy storage materials

| | |
|-------------------------------|--|
| Journal: | <i>CrystEngComm</i> |
| Manuscript ID | CE-ART-07-2015-001369.R3 |
| Article Type: | Paper |
| Date Submitted by the Author: | 27-Oct-2015 |
| Complete List of Authors: | Barik, Rasmita; Institute of Minerals and Materials Technology, Hydrometallurgy Mohapatra, Mamata; IMMT, H & EM Dept.; University of Waterloo, Department of chemistry |
| | |

Solvent mediated surface engineering of α -Fe₂O₃ nano materials: Facet sensitive energy storage materials

*Rasmita Barik, Mamata Mohapatra**

Hydro & Electrometallurgy Department, CSIR- Institute of Minerals and Materials Technology, Bhubaneswar- 751 013, Odisha, India

KEYWORDS : Ethylene glycol, Crystal facets, Pseudo capacitance

ABSTRACT: Surface-chemical properties of iron oxide nano materials are keenly studied to explore them for many futuristic applications. Therefore many synthetic strategies are being now pursued to develop unique morphology with active surface and unusual crystal facets for advance uses. Here a novel processes for the formation of α -Fe₂O₃ phase have been established by a facile solvent mediated precipitation routes. Ethylene glycol has been used as solvent which plays an active role to control surface morphology and orientation of facets during crystal growth. The effect of various parameters on the morphology, structure of the product, and electrochemical properties were studied. Mainly high surface energy facets were stabilized in high concentration EG in reaction solution. Formation of (012) or (001) facets were observed in the reaction solution of lower concentration of EG. Hematite with flowery morphology having (012) plane orientation has been achieved by the assembly of pseudo cubes with (012) facets and a secondary growth process. The sample obtained at Fe:EG 1:2 shows ultra-high pseudo capacitance value of 450 F/g with related to high surface area. The present study can be further explored for the preparation of other functional oxides with new active facets for energy storage applications.

▪ INTRODUCTION

The extensive research on solution-based crystallization processes for the synthesis of next generation affordable materials is highly motivated to get intriguing surface characteristics. Nobel synthetic strategies are mainly focused to manipulate shape, orientation, growth, direction and stability of high energy facets of crystals. Solvents and ligands stand specifically to control growth and self-assembling of nano crystals. Because of their dynamic role on regulating different physical forces such as van der Waals, electrostatic, and entropic forces in the formation of super lattices. Thus, their presence can lead to formation of new class of nanostructured solid materials. Optimizing their concentration, reaction time and temperature during solvent-dependent hydrolysis of metal ions facilitates engineering of different crystallite with facets¹. Realizing the importance of activities of crystals at nano-scale level for future usage numerous synthetic methods are developed to generate new functionalized low cost environmentally benign materials. Notably, various well defined α -Fe₂O₃ nanocrystals have been actively investigated for size or morphology-dependent properties² and have been attempted for potential applications in the field of sensors,³⁻⁵ photocatalysts,⁶⁻⁸ waste-water treatment,^{9,10} photo-electrochemical cell,¹¹ lithium ion batteries,^{12,13} and super capacitors¹⁴⁻¹⁷. Besides that these materials have also tendency to form stable ordered superstructures as meso-crystals¹³. Hierarchical ordered structural features plays a pivotal role for the construct multifunctional materials. However, fabrication of the meso crystals with particular facets is challenged by the thermodynamic growth mechanisms of crystals as these can easily fuse to a single crystal¹³. Thus, the Fe₂O₃ mesocrystals with high-energy exposed facets are desirable for improved multifunctional properties. Duan *et al.*¹³ employed a facile solvothermal approach to prepare high-stability rhombic hematite meso crystals using N,N-dimethyl formamide (DMF) and methanol as the mixed solvent. Cai *et al.*¹⁸ explored the possibility of top-down fabrication of hierarchical micro cones and micro discs hematite meso crystals with controlled shapes through chemical etching.¹⁸ We report herein a facile and scalable hydrolysis method to prepare different facet oriented hematite meso-crystals with ethylene glycol or 1,2-diol as the solvent. It was demonstrated that the meso crystals were composed of cubic nanoparticles with good crystallinity and uniform size distribution. The solvent, due to their ligation ability, served as a connector or binder to assemble the Fe(OH)₃ into the unique morphology depending on the concentration of the reactant solution that was inherited in the final mesocrystal. Further the

resulting facet oriented mesocrystals have shown shape dependent pseudo capacitive performances.

▪ EXPERIMENTAL SECTION

Synthesis of Fe₂O₃ mesocrystals and nanoparticles. Iron nitrate Fe(NO₃)₃ and 1,2-diols (EG) were purchased from E-Merck, India and used without further purification. In a typical experiment, equal amount of 0.1M solutions of iron nitrate and EG was homogenized under vigorous stirring. The homogeneous mixed solution was then heated at desired temperature and brown precipitate was generated after certain interval of time. The solid product was collected by centrifugation (8000 rpm) and was washed using deionized water for several times till free of nitrate and then was dried at 60°C for 8h. The sample was named as FeEG₁. Similarly, a series of experiments was carefully designed with different ratios of precursor solutions, keeping other controlled parameters (reaction temperature, time, cleaning procedures and drying temperature) fixed,. The samples prepared by varying the ratio of iron nitrate: EG as 3:1, 2:1, 1:2, 1:3 and 1:4 and were coded as FeEG_{0.25}, FeEG_{0.5}, FeEG₂, FeEG₃, and FeEG₄.

▪ MATERIAL CHARACTERIZATION

All the samples were characterized by using various analytical techniques and spectroscopic measurements. Iron was analyzed by volumetric method using BDAS indicator. To identify the crystal structures of the synthesized materials, XRD patterns were recorded with an automated Siemens D-5000 Diffractometer using Mo K α ($\lambda = 1.79 \text{ \AA}$) radiation. The FTIR spectra were taken using NICOLET-670 Spectrometer. The Raman spectra were taken using a Renishaw in via micro Raman Spectrometer (Renishawplc, Gloucestershire, UK) equipped with a 514 nm green laser having 1 cm⁻¹ spectral resolution of Raman shift, X–Y step resolution of 0.1 μm and confocal resolution of 2.5 μm . The surface morphology and microstructure of the products were examined by Transmission electron microscope (TEM) (FEI, TECNAI G2 20, TWIN) operating at 200 kV, equipped with a GATAN CCD camera. The Brunauer–Emmett–Teller (BET) surface areas were carried out in Autosorb-iQ and ASiQ-WiN device from Quanta chrome. UV–Vis absorption measurements were carried out with Perkin Elmer Lambda-35. Cyclic-voltammograms were recorded using a computer controlled CHI660C electrochemical analyser (CHI, USA). Electrochemical analyses were performed using three-electrode cell with a glassy

carbon working electrode (area 0.07 cm^2), a platinum auxiliary electrode and Ag/AgCl (0.1M Na_2SO_4) as reference electrode in the potential range of -1 V to 1 V under a sweep rate of 5-100 mV/s. All the electrochemical experiments were carried out in an argon atmosphere. The required amount of as-synthesized materials were well dispersed with 0.1ml of 2% Nafion. Calculated amount of dispersed solution was dropped on tip of the glassy carbon electrode and was dried under nitrogen atmosphere prior to electrochemical experiments. Cyclic voltammetry studies (CVs) for some of the samples were performed. Charge-discharge tests were carried out in same voltage range using chrono-potentiometric method.

▪ Results and Discussion

XRD analysis. The XRD patterns of the as synthesized samples obtained at different time interval with the precursor ratio Fe:EG of 1:1 under reaction temperature of $95 \pm 5^\circ\text{C}$ (labeled as 100°C) are given in Figure 1. The physico-chemical analysis were given in supporting information Figure S₁. It may be noted that the samples were collected at 1h and 2h were of jelly type. Actual precipitation started after 2h. All the diffraction lines were matched to hematite phase (JCPDS file Ref. no. 00-024-0072, with rhombohedral crystal system and Space group R-3c). Presence of different planes (012), (104), (110), (113), (018), (024), (116), (214), (300), (2114) and (0114) confirmed the purity of the phase. The XRD pattern showed that the prepared sample might be monophasic, free of other impurities. Closer inspection of the diffractograms showed (Figure 1b) that the intensities of the (104) Bragg reflection becomes relatively enhanced with progress of time. This becomes particularly clear when comparing the relative intensities of the (104) reflection with that of the (110) reflection; initially the (110) peak intensity was more than that of (104) peak.

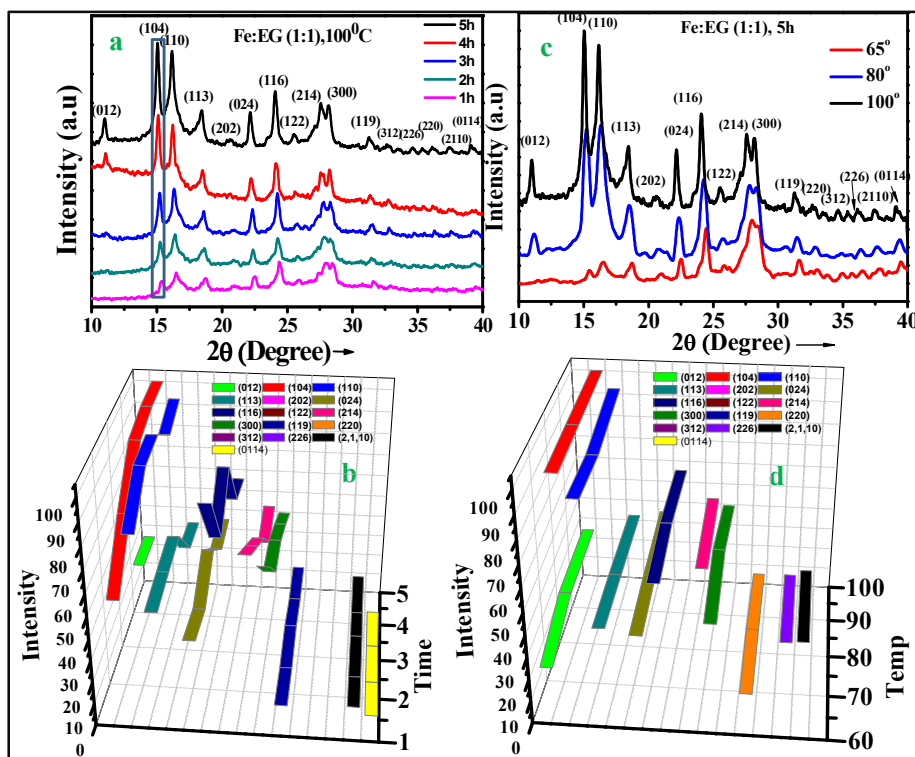


Figure 1. XRD patterns of samples with Fe: EG ratio 1:1 **(a)** under different reaction times, **(b)** corresponding intensities of different planes, **(c)** XRD patterns obtained at different temperature and **(d)** corresponding intensities of different planes.

Gradual increasing the reaction time, the (104) peak was larger than the (110) peak. Again it was observed that, X-ray peak broadening with the $(hk0)$ peaks being sharper than the (hkl) peaks which was due to stack of thin crystalline plates (discs or cube) for better crystal development in the basal plane ‘ a ’ than along the (hexagonal) ‘ c ’ direction.¹² However, the preferred orientation could be depicted from diffraction peak intensity ratio of the (110) with respect to the (104), as it was distinctly deviated and having more value from the standard ratio of 0.7. The discrepancy of intensity ratio was due to the different exposing facets of the assembly units with exposure of (110) facets during crystallographic orientation. For the 2 h sample, the (012) and (220) peaks were barely visible, whereas the same were gradually developed in the subsequent samples. The same trend was also seen for the (2110) and (310) peaks.

Effect of temperature on phase formation is shown in Figure 1c. As shown in XRD patterns of samples, the characteristic peaks could be indexed only to hematite phase and mostly similar trends of development of peaks were observed when compared to that observed during time variation. It has been clearly observed without using any other foreign reagent for pH adjustment, hematite phase was formed in presence of EG solvent. Previously many authors have also reported the synthesis of hematite¹⁹⁻³⁰ using ethylene glycol (EG) during synthesis with different salt of iron and other precipitating agents at high temperature or using surfactant or polymers followed by post heat treatment. The growth orientation of hematite developed using EG was reported in the (110), (104) and (300) lattice.¹⁹⁻³⁰ Table S₁ was shown regarding the synthesis of various shape of hematite particles and their properties studied using EG as solvent.

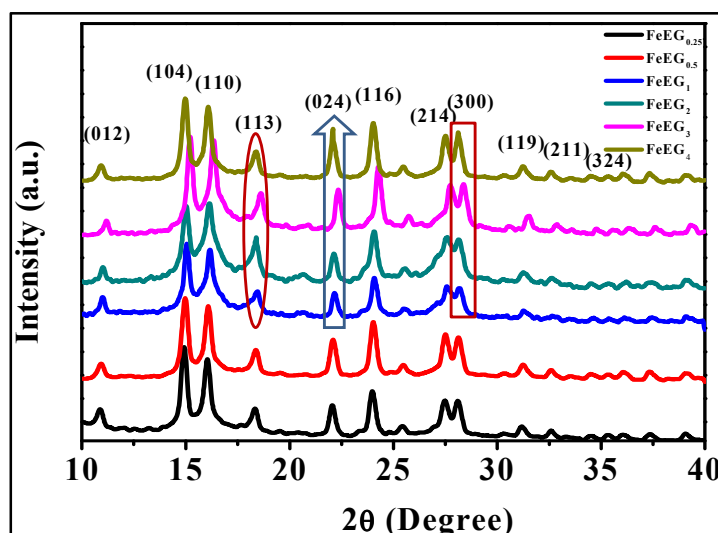


Figure 2. XRD patterns of samples with different Fe: EG ratio. Discrepancies in the intensities of different peaks are shown in corresponding highlighted box.

The effect of EG on the phase formation by varying Fe: EG ratios are shown in Figure 2. It is observed that concentration of EG did not affect the formation of hematite phase as there was no other peaks present in all the samples, but distinctly affected intensity of various peaks. The peak intensity of (113) plane for the sample obtained at 1:2 showed higher intensity than the other samples. Similarly the (024) and (300) peaks of the sample obtained at 1:3 ratios were comparatively intense and further their intensity was

remarkably enhanced for the sample obtained at 1:4 ratio. From these observations, one can conclude that presence of EG definitely affects the orientation of hematite planes which might change the morphology of the particle and surface area due to development of preferred facets. Further, TEM study enlightened more on morphology dependency on the concentration of EG.

The XRD Study was supported by FTIR and Raman study (given in supporting Figure S₂ and S₃).

Effect of time on nanostructure of hematite particles keeping Fe: EG as 1:1. The formation process and growth of the samples prepared at various time with Fe: EG ratio 1:1 are shown in Figure S₄ (supporting information). The hematite particles with pseudo cubic embryos emerged from fine amorphous particles, as clearly shown in TEM image for the sample at 2 h. With the further increase in reaction time to 3 h, more perfect features and dense particles were observed due to self-assembling of the particles. Particles were distinctly assembled to a particular orientation and growth of the size is observed in the TEM of the sample achieved at 5 h. In contrast to our observation, the structure of the hematite reported by earlier work, obtained using EG along with other precipitating agents were of rod, spindle or flowery shapes.¹⁹⁻³⁰ The TEM image at 5 h showed that particles were assembled as sea nodules or pseudo-hexagonal shape along with few rods indicating the presence of homogeneous nanocrystals with an average edge length of 5–10 nm. Further the role of solvent on shape of the hematite particles was investigated.

Effect of Fe:EG ratio on nanostructure of hematite particles. To study the samples obtained at different ratios of Fe: EG are given in Figure 3 and 4. Cubic particles were “fused” together forming a pseudo structure for the sample obtained at Fe:EG ratio 1:1. These samples were composed of many quasi-cubic nanocrystals as seen visually. Closer inspection of TEM by enlarged images confirms (corresponding inset Figure 3 the pores and hierarchical structure and have clear edges and shape outline. There were still small amount of smaller nanoparticles visible on the surface of the pseudo cube. The size

of the nano particles showed that the edges were slightly etched, and cracks appeared on the edges as revealed by the zoom-in view. Outlines were used to highlight the edges of typical particle.

From the corresponding SAED pattern, the diffraction spots could be attributed to (012), (104), (110), (113) and (024) planes and/or their equivalent planes under the incident electron beam along the (111) direction. HRTEM showed that, unlike the perfect cubes with dihedral angles of 90° , the crystals might not be enclosed by low-index surfaces such as (100) or (001). The observation from the TEM obtained for the sample obtained at Fe:EG =1:2 suggest that the overall morphology and size of the nanostructured material was completely different. The pseudo cubes were assembled and flower like hierarchical structures were constructed by a large number of pseudo cube particles.

The continuous fringes shown in SAED patterns between the aggregated particles indicated that the aggregation of small particles were not random but in an ordered manner with the same crystallographic orientation. The corresponding HRTEM image of the selected area showed crystalline character with a lattice spacing of 0.39 nm, which was consistent with (012) lattice plane of $\alpha\text{-Fe}_2\text{O}_3$ and the mesoscopic structure has exposed (012) planes, indicating that the second order of the primary particles can be assigned to oriented attachment. The crystallographic orientation on (012) planes may be due to adsorption of hydrolysis product of ethylene glycol on O-terminated layer of (012) plane. Complexation of EG with oxygen terminated surfaces is feasible due to hydroxylation ability of above surface which can stabilize the high-energy (012) planes.^{31,32}

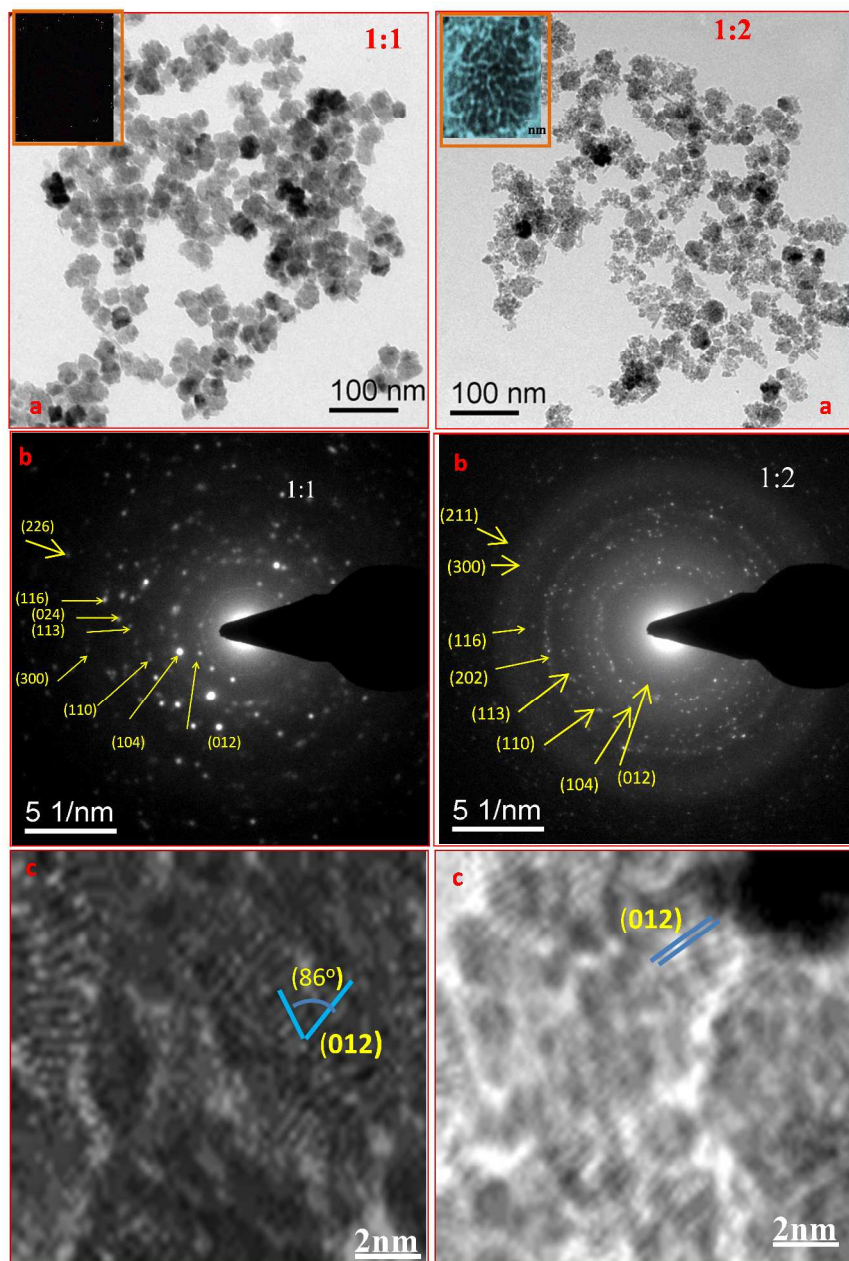


Figure 3. TEM images showing the size and shape evolution of α - Fe_2O_3 nanocrystals for Fe:EG ratio(1:1) and (1:2), (a) TEM image showing particle shape as inset, (b) corresponding diffraction pattern showing planes and (c) HRTEM image showing orientation of particles in different planes.

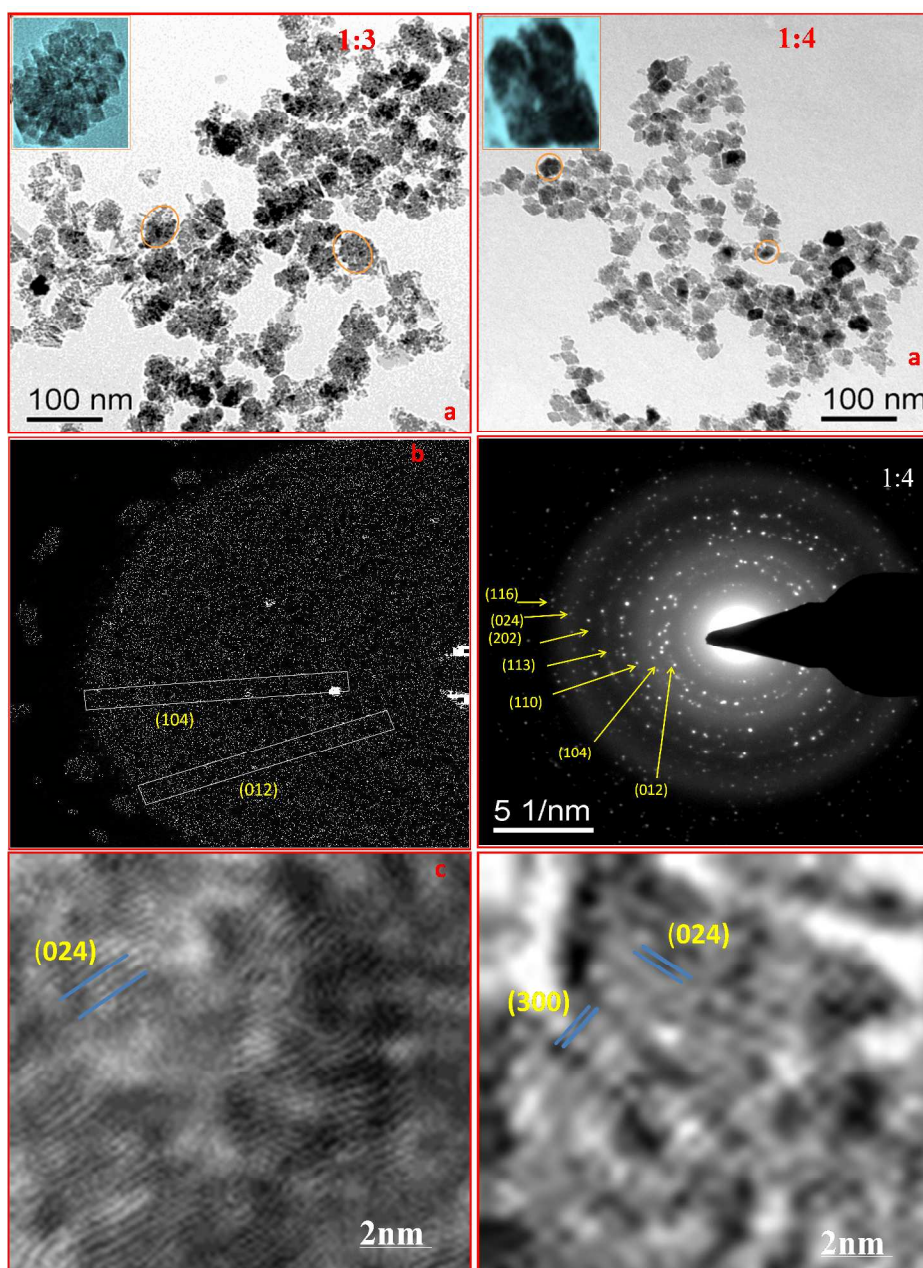


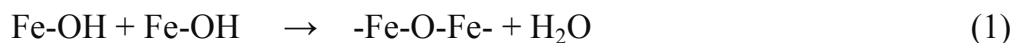
Figure 4. TEM images showing the size and shape evolution of α -Fe₂O₃ nanocrystals as a function of Fe:EG ratio(1:3) and (1:4),(a) TEM image showing particle shape as inset,(b) corresponding diffraction pattern showing planes and (c) HRTEM image showing orientation of particles in different planes.

By increasing Fe:EG ratio to 1:3 the orientation of pseudo cube change to ellipsoidal form. The spindle-like morphology of samples is shown in corresponding inset Figure. TEM image showed that the average length and diameter of the structures were

approximately 180 and 120 nm respectively. The corresponding high-resolution image of the spindles indicates (024) parallel lattice planes of α -Fe₂O₃ nanocrystals. The selected-area electron diffraction (SAED) pattern revealed the single-crystalline nature of the sample and the linear arrays of dots are from parallel sets of (116) and (104) planes. This apparent single-crystalline nature arises due the release of previously surface-attached molecules by crystallographic fusion with elimination of two high-energy surfaces. From TEM image of the sample obtained at Fe:EG 1:4 ratio, several fused pseudo cube in concave shape could be clearly observed. The lateral face of the cube is showing concavity in nature as shown in corresponding inset Figure. SAED pattern shows highly crystalline nature. High resolution TEM image of an individual particle showed (300) and (024) planes. Similar type of growth of concave nano cubes in cubic crystal systems were observed by Liang *et al.*³³ They attributed this type of growth to facet-selective capping or kinetic controlled overgrowth. Thus, after a careful investigation of the nanostructure of the products in different Fe:EG ratio, It is found that the morphology evolutions of hematite nanoparticles are significantly different and can be attributed to the concentration and reactivity, adsorptivity of EG on formation and growth rate of different facet of hematite particles. Even, the synthesis of concave hematite particle is feasible which is in general considerably difficult due to their more complicated structures and stronger metal–oxygen bonds.

Mechanism. It is speculated that the formation of α -Fe₂O₃ with different morphologies is due to an orientation crystallization mechanism as shown in supporting Figure S₅. In the first step, the Fe-glycolate complexes are formed by the addition of EG aqueous solution to the Fe³⁺ containing solution (the molar ratio of the EG-complexed and uncomplexed Fe ions depends on the employed [EG]/[Fe]). During hydrolysis, the alkoxide groups (-OR) are replaced via the nucleophilic attack of the oxygen atom of a water molecule with the release of alcohol and the formation of a metal hydroxide. Condensation reaction between two hydroxylated metal species leads to the formation of M–O–M bonds upon release of water (oxolation), whereas the reaction between a

hydroxide and an alkoxide leads to the formation of –Fe–O–Fe–polymeric network upon release of an alcohol (alkoxolation). Then, it is dehydrated due to solvation by EG, which results in the formation of –Fe–O–Fe bonding (Equation 1) and extends to form the iron hydroxide nucleus by precipitation of the ferric ions.



Iron oxide has high tendency toward the oriented attachment growth via electrostatic interactions to control the aggregation process.³⁴ α -Fe₂O₃ has corundum structure where the surface hydroxyl group configuration of the various crystallographic planes such as (100), (110), (012), (104) and (001) for hematite was quite different.³⁵ For (001) planes, the surface hydroxyl groups are all doubly coordinated whereas for other planes that commonly occur at the surface of natural and artificial hematite crystals, such as the (100), (110), (012), and (104) planes, singly coordinated surface hydroxyl groups.³⁶ Therefore, the electrostatic attraction and affinities for hematite exposed facets are much higher for the (100), (110), (012), and (104) planes than for the (001) plane. In this case, the electrostatic force between particles is caused either by the charged particles or by the charge separation on {104} polar facets. The strong interaction between nuclei leads to a fast attachment for self-organized nano flower-like particles in solution with directionally attached to each other by compulsorily overcoming the strong electrostatic repulsion on their (001) planes to minimize the total Gibbs energy of the system. The orientation of nano flowery shape may be ascribed to slow and confined growth along the (0001) direction is inherently because of the low surface energy of this plane and inherent polar crystallographic structure of α -Fe₂O₃ in the organic solvent.³⁷

In general, in hematite structure, Fe³⁺ and O²⁻ ions are arranged alternatively along the *c* axis.³⁸ The larger up/down surfaces are terminated either of them and there are net ionic charges on either surface. Therefore, (0001) planes terminated by iron atoms may favorably be bonded by EG due to nucleophilic affinity to surface and the growth along (0001) directions were confined and large (0001) facets appear. However, the fully

terminated (012) surfaces are covered by mono- or three-coordinated oxygen atoms with which the oxygen atom of EG has an electrostatic repulsion. Thus, the vertical growth along the *c*-axis is confined, but the radial one along the *ab*-plane is enhanced. And consequently the growth of the flower like assembled structure is achieved. However, with the addition of more EG into the reaction system, an intermediate connection is developed due to bridging of one terminating oxygen atom on a (012) surface and EG molecule through hydrogen bonding. Thus growth along *ab*-planes were retarded and more (012) terminated facets appeared as shown in Figure 5(i). With further increase of concentration of EG, formation of concave nano cubes may be obtained due to facet selective capping during kinetically controlled process due to diffusion of precursor from solution to the surface and the growth rate at which atoms were generated and added to the surface of a growing seed. When EG concentration was more, there will be a gradient for the precursor concentration from high to low corresponding to the area from bulk solution to the surface of the seeds.

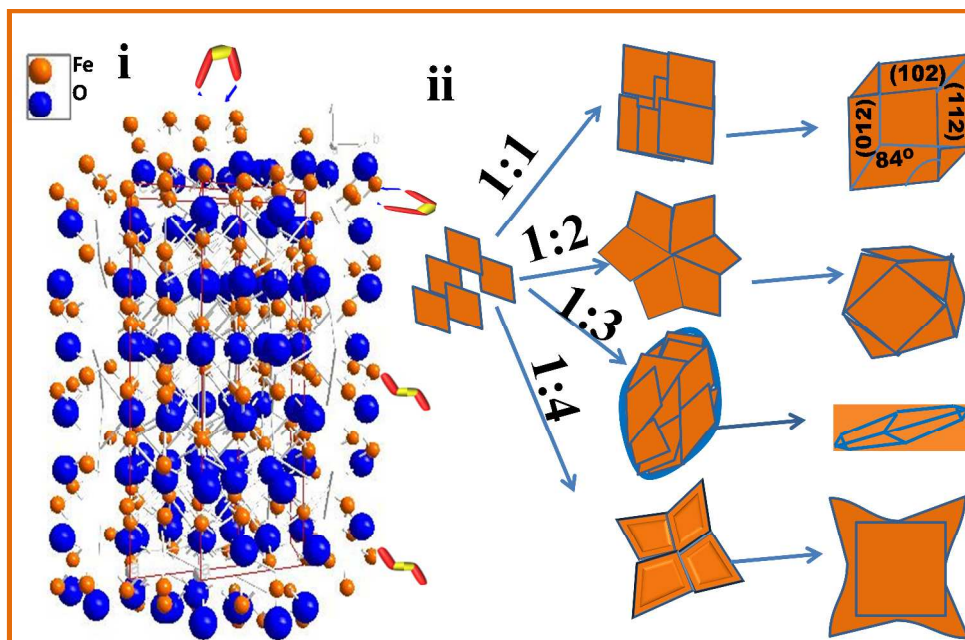


Figure 5. (i) Illustration of surface termination types of hematite (024) attachment of EG on surface. Oxygen atoms are in blue, and iron atoms are in brick red and (ii)

The geometric models of different shape of hematite obtained at various ratio of Fe:EG and their orientated attachment.

Under this condition the atom generated on the surface of nano cube would be preferentially added to the site with the highest reactivity owing to an insufficient supply of atoms, and for cubic particle, the eight corners have the highest reactivity. Herein, the dissolution of iron ions and subsequent formation of the iron-EG complexes play a key role in the kinetic growth process. The EG dependent assembling of pseudo cube for preferential faceted growth and orientation of the hematite particles are shown in Figure 5(ii).

Surface area analysis. Surface area of samples mainly depends on size and shape of particles. High surface area with manipulated structure plays a vital role for property evaluation of nanostructured materials. N_2 adsorption desorption isotherm as shown in Figure 6a measurements are carried out to determine the surface area and pore structure of the samples. The Brunauer–Emmett–Teller (BET) surface areas of the samples obtained at 65°C, 80°C, 100°C for Fe:EG= 1:1 and for Fe:EG=1:2, 1:3 and 1:4 ratios are found to be 134.95, 81.14, 67.47, 72.94, 63.72 and 37.04 m^2/g respectively. With the increase in synthesis temperature for the prepared samples the surface area value decreased. With the increase in temperature, the formation of large and compact structures took place which leads to a reduction of the surface area to volume ratio. When the Fe:EG ratio was varied from 1:1 to 1:2 the surface area increased and after that decrease in trend was observed. The surface area of the synthesized samples are much higher as compared to reported values.^{20,24,39-45} Typical N_2 adsorption/desorption isotherms of samples obtained at various Fe:EG ratios are given in Figure 8a. There is a distinct hysteresis in the $P/P_0 > 0.5$ region of the isotherm observed for the samples prepared at 1:2 and 1:3 ratios, indicating the presence of mesopores formed by the porous stacking of nanostructured crystals. The hysteresis loop shifted to a higher relative pressure on approaching $P/P_0 = 1$ confirming the mesoporosity of the sample along with low degree of aggregation.

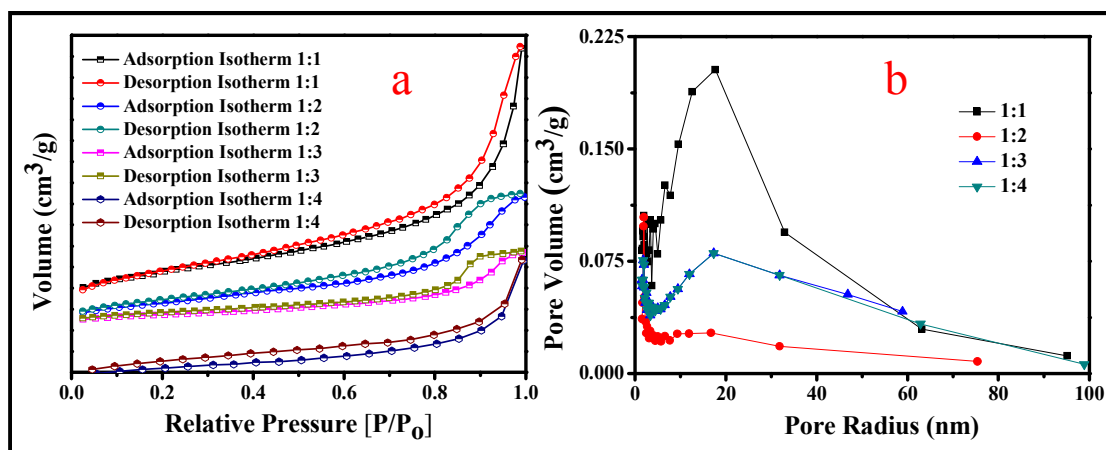


Figure 6. (a) N_2 adsorption/desorption isotherms, (b) Pore size distributions for hematite samples derived from desorption branches of N_2 for hematite samples obtained at different ratio of Fe:EG.

The observed isotherms can be classified as Brunauer-Deming-Deming-Teller or BDDT, type I and IV isotherms and H3-type hysteresis loop in the IUPAC classification.⁴⁶ This classification suggests the presence of the open slit-shaped capillaries with very wide bodies and narrow short necks in these materials. In contrast, the isotherms of the other two materials display only a negligible adsorption of nitrogen in the low P/P_0 region and no significant hysteresis in the mid P/P_0 region. This observation indicates small populations of micropores and mesopores in these materials. Thin hysteresis loop was due to the slight capillary phenomenon existing within the very loose nano architectures. But when the Fe:EG ratio is increased to 1:4 the hysteresis behaviour changed which can be attributed to the closing of the pores by iron oxide.^{47,48} The pore size obtained by Barrett-Joyner-Halenda (BJH) (shown in Figure 6b) method under the above mentioned conditions varied between 10-30 nm. Pore volume of the samples were found to be 0.0194, 0.045, 0.08661 and 0.09693(cm^3/g) for Fe:EG ratio 1:1, 1:2, 1:3, and 1:4 respectively. The increasing pore volume corresponds to the increasing core size of the self-assembling of pseudo-cubic structure with increasing Fe:EG ratio. The extraordinary BET surface area values of synthesized α - Fe_2O_3 nanostructures provide a fine example to study the size-dependent properties such as supercapacitor and gas sensor.⁴² The high BET surface area is beneficial for adsorption

and for various catalytic reactions. More the surface area more will the unsaturated surface coordination sites exposed to the gas, which enable storage of more gas molecules and shows a better sensing capacity.⁴²

Optical properties of synthesized α -Fe₂O₃ samples at various ratios of Fe:EG. The optical absorption properties of the as-prepared α -Fe₂O₃ samples were investigated at room temperature by the UV-Vis spectra and have been represented in Figure 7a. Depending on the size and shape of the particles the nature of absorption varies. In general, α -Fe₂O₃ nanoparticles exhibit strong absorption in the range of 200–400 nm in the UV region and weak absorption at 400–800 nm of the visible region. The two types of optical absorptions in the UV and visible regions are mainly attributed to the two kinds of electronic transition mechanisms. The former is due to the contribution of the direct charge transition of $O_2^- 2p \rightarrow Fe^{3+} 3d$ (UV absorption), and the latter originates from the indirect charge transition of $Fe^{3+} 3d \rightarrow 3d$ (visible absorption).⁴⁹⁻⁵⁰ For sample FeEG₁, it revealed that two absorption edges around with sharp edge at 394 nm and broad spectrum at 530 to 550 nm may be due to superimposing of scattering of visible light on the absorption of as-prepared architectures, which were consistent with the reported hematite NPs.^{51,52} As the ratio of Fe:EG increased, blue shifting of adsorption edge at 394nm is observed. This blue-shift for hematite nanoparticles was also observed due to size reduction,⁵³⁻⁵⁴ morphology change from nanotube to nanoring⁵⁵ and finite size effect.⁵⁶ Moreover, the blue-shift of the absorption band due to pair excitation is shape-dependent as well when the particle size is comparable with the incident wavelength. It can also be explained in terms of the ionic bond strength between metal ions and oxygen ions which affected the electronic transition for the charge localized to the FeO₆ coordination site (e.g., Fe^{3+} ligand field and $O^{2-} \rightarrow Fe^{3+}$ charge transfer transition) and the adjacent Fe^{3+} cations. Again it was observed that the absorbance peaks around 520 to 550 nm are gradually reduced with increase in Fe:EG ratio. This change in the degree of transition depended on the shape and size of the particles. It may be mentioned here that the aggregated nanostructure are reduced with formation of defined and orientated

structure as the Fe:EG ratio increased, therefore, the transition at 520-550 nm is reducing. In case of the concave type hematite synthesised at 1:4 ratio, another UV-Vis band located in the far-UV region from 275 to 285 nm with intense broadband is additionally observed. This band can be a contribution of tetrahedral (Td) or defectively coordinated ferric cations similar to strong charge transfer band observed in a defective environment.⁵⁷ To determine the type and value of the optical gaps of as synthesized hematite particles, The Tauc–Mott (TM) plots were derived from the absorption spectra according to the equation mentioned below

$$(\alpha E_{ph})^n = B(E_{ph} - E_g) \quad (2)$$

Where α is the absorption coefficient, E_g is the optical energy gap, B is a constant, E_{ph} is the photon energy ($E_{ph}=h\nu$) of the incident light and n is an index characterizing the type of optical transition: n equals 2 for allowed direct transition and 0.5 for allowed indirect transitions. The optical band gaps are obtained from the intercept of the best linear parts of the curves near the band edge with $(\alpha E_{ph})^n = 0.1$. For suspensions of NPs used $\alpha = A/c$, where c is concentration of NPs in g/L. The TM plots for the baseline corrected spectra for direct band gap (Figure 7b) showing the band gap values as inset, which increases gradually from 1.91 to 2.4 with increase in Fe:EG ratio. The band gap values for our hematite particles are smaller as compared to the values reported for the direct band gap of nano particulate hematite and hematite films [⁵⁸ and references there in]. As such the narrower band gap is due to lower energy of the valence band edges imply a higher electron affinity and higher oxidation power of their thermalized or photo generated holes.⁵⁸ The trend in increase in band gap due to solvent concentration may be due to stabilization of high energy facet in hematite particle.

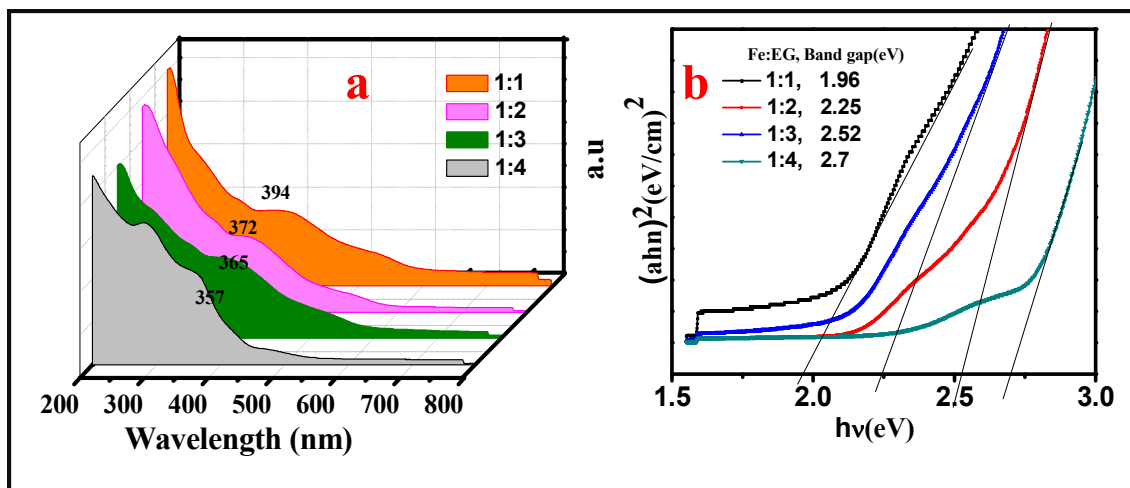
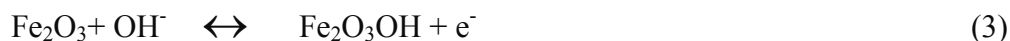


Figure 7. (a) UV-visible absorption spectra of synthesized samples prepared at different ratio of Fe:EG at 100°C for 5 h and (b) plot of $(\alpha h\nu)^2$ versus photon energy for direct transition.

Electrochemical properties of synthesized α -Fe₂O₃ samples at various ratios of Fe:EG. α -Fe₂O₃ has been considered as one of the promising materials for supercapacitors due to their high conductivity at room temperature. The specific capacitance (SC) of iron oxide electrodes is strongly influenced by the surface morphology, surface area, porosity etc. which can be tuned by modifying synthetic routes. In our present approach, hematite particles with different morphologies and facets have been prepared successfully and to see their electrochemical properties cyclic voltammetry studies were conducted. Generally, the capacitance mainly derived from the pseudo capacitive charging and discharging based on the following reversible redox reaction:



The cathodic peak may be attributed to the reduction of Fe(III) to Fe(OH)₂, whereas the anodic peak corresponds to the oxidation of Fe(OH)₂ to Fe(III).

The cyclic voltammetry (CV) curves recorded from -1 to 0.8 V in 0.1M Na₂SO₄ solution with a Pt counter-electrode and a Ag/AgCl reference electrode (following the procedure explained in experimental section) for as-prepared hematite samples are shown

in Figure 8. It can be clearly observed that there is a distinct pair of redox peaks during the anodic and cathodic sweeps. The shape of the CV curves suggests a pseudo capacitive characteristic; distinctly different from normal electric double-layer capacitance with a rectangular CV shape. It indicates the existence of Faradic processes, which is a signature of pseudo-capacitance. It should be noted that the shape of CV at 100 mV/s is almost symmetrical. The charge storage in the Faradic process is achieved by an electron transfer that produces chemical or oxidation state changes in the electro active materials according to Faraday's law related to the potential.

The cathodic peak shifts to lower potentials and also the anodic peak is shifted to the higher potentials. It may be due to the reversible reaction of process of Fe^{3+} and Fe^0 . Herein the current density for the Fe_2O_3 is larger than that of the blank electrode which shows the higher capacity and faster kinetics for transformation in the electrode.⁵⁹⁻⁶⁰ With the increasing in the scan rate, polarization increases, so there should be a shift in the position of the oxidation and reduction peaks.⁶¹ But when the synthesis temperature is increased up to 100°C the visibility of the cathodic peak is less. With the increase in scan rate the current increases which affects the hysteresis of the cathodic and anodic peaks. The samples synthesized at 100°C shows pseudo capacitance behaviour curves have retained their configurations with the increase of sweep rate. Due to the resistance of the electrode, a positive shift of oxidation peaks and a negative shift of reduction peaks are observed.⁶¹ The specific capacitance value decreased with increase in scan rate. The decrease in specific capacitance is attributed to diffusion limits of electrolyte ions. Only the outer active surface is responsible for charge storage, while the inner active sites cannot sustain the redox transitions. The decrease in capacitance suggests that parts of the surface of the electrode are inaccessible at high charging-discharging rates. The formation of Fe_2O_3 in EG medium provide extra OH to the system which causes higher potentials thus by increasing potential, current rapidly increases and faster growth of Fe_2O_3 takes place.⁶² Interaction of EG on hematite surface affects depletion of electrode resulting from dissolving oxide species in the electrolyte which causes the redox behaviour of iron.⁶³

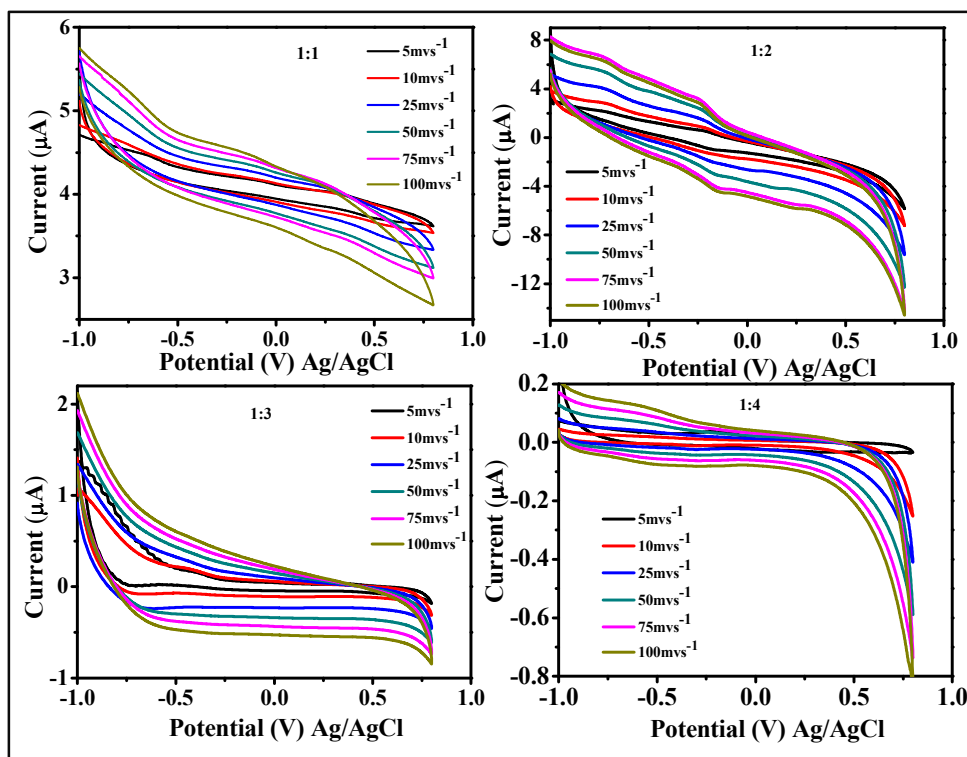


Figure 8. Cyclic voltammograms of α -Fe₂O₃ nanostructures synthesized at different ratio at different scan rates (5–100 mV/s) in 0.1 M Na₂SO₄ electrolytes in a three-electrode electrochemical cell.

All the samples showing quasi-rectangular CV curves for a wide scan range of 5–100 mV/s. The current increased with the scan rate as expected, while the CV curves lost the rectangular shape when the applied scan rates were higher. This is due to the kinetics of electron transportation in the electrode materials and the limited ion adsorption–desorption at electrode and electrolyte interface. The capacitive results of the hematite samples obtained at 1:3 and 1:4 showing the presence of pseudo capacitive characteristics. The current attained for the sample Fe:EG (1:2) nano iron oxide is higher than others. The CV curves with increasing scan rates exhibit a gradual deviation from the rectangular shape owing to both EDL capacitance and pseudocapacitance characteristics. At present, there are three accepted mechanisms of charge storage for pseudo capacitor electrodes.⁵⁹

The first, which is generally accepted to occur for all charged metal or metal oxide surfaces, involves the adsorption of ions from the electrolyte as a monolayer on the

electrode surface. This effect may be manifested through the under potential deposition of cations or through partial charge transfer between the metal centres of the electrode and electrolyte anions, the so-called electro sorption valency.^{64,65} The second mechanism of pseudocapacitance involves redox reactions at the surface of the electrode such as proton exchange in the amorphous surface and the third relies on the fast reversible intercalation of ions into the bulk of the material.^{22,66} Whereas all of these mechanisms can be described as pseudo capacitive owing to changes in the oxidation state of the transition metal, only electro sorption valence has been demonstrated as an anion effect.

The voltammetric charge integrated from a positive or negative scan of CV can be used as an effective signal in determining the pseudocapacitance. Accordingly, the average specific capacitance (C_s) of the sample is assessed by the following equation.⁶⁵

$$C_s = I\Delta t/m\Delta V \quad (4)$$

Where I is the discharge current, Δt is the discharging time period in seconds m is the mass of the electro active materials and ΔV is the potential difference. At low scan rate, H_2O can be easily diffused into the electrode. At high scan rate, H_2O will only approach the outer surface of the electrode, and the effective interaction between the ions and the electrode is greatly reduced. The material located in the inner has little contribution to the capacitance.⁶⁵ The increase in the specific capacitance at the lower scan rates is mainly due to the fact that nearly all the active electrode surface is available for efficient intercalation. The calculated values of specific capacitance for the samples obtained at different ratio of Fe:EG are given in Figure 9. The variation in Fe:EG ratio plays the more vital role to manipulate the specific capacitance value. As the Fe:EG ratio increases the specific capacitance value also increased up to 1:2 ratio and then decreased with changing of the nature of supercapacitance. The FeEG₂ sample with Fe:EG ratio 1:2 is showing unanimously high value (450 F/g) as compared to other samples. These values are high in comparison with the values reported in the literature for α -Fe₂O₃ samples with different morphologies varying from mesoporous to nano tubes [^{22,67-69}]. From the above

analysis, it is concluded that the performance of present synthesized hematite samples as electrode have been greatly affected by their shape and facets.

The CV measurements of comparison plot for the hematite nano-composites with variation of Fe: EG ratios are shown in Figure 10a. The charge-discharge plot for the Fe: EG (1:2) sample with current density 5 mA g^{-1} was shown in Fig 10b inset. The iron oxide supercapacitor exhibits good electrochemical capacitance performance obtained by a linear variation of the voltage during the charging–discharging process. The cycling stability was examined for 500 cycles at a specific current density of 100 mA g^{-1} was given in Fig 10b. The specific capacitance decreased slightly after 300 cycles.

Basically, charge storage is surface process, which involves adsorption/desorption or intercalation/deintercalation of proton/ alkali cations into the bulk oxide particles with concomitant reduction/oxidation of the iron cations. In the present study, the redox process may be governed by the adsorption and desorption of proton/ alkali cations into the hematite matrix. So the FeEG₂ sample with the larger surface area shows the highest specific capacitance value.

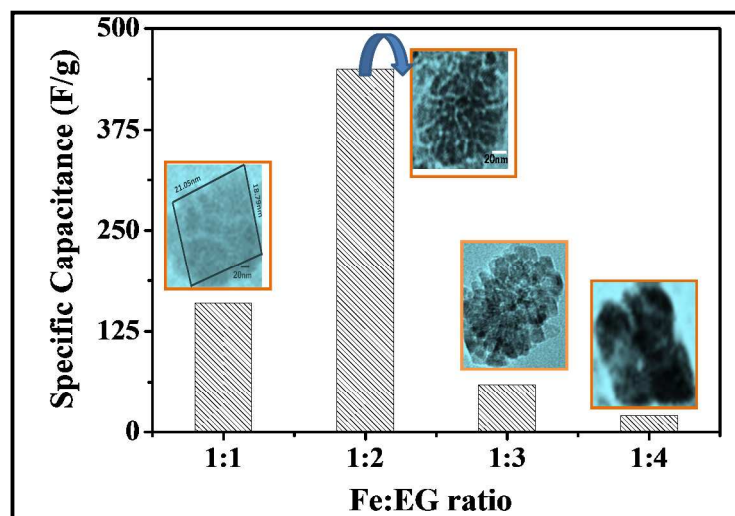


Figure 9. Specific capacitance at scan rate of 100 mV/s of $\alpha\text{-Fe}_2\text{O}_3$ nano crystals with different shapes obtained by variation of Fe:EG ratio.

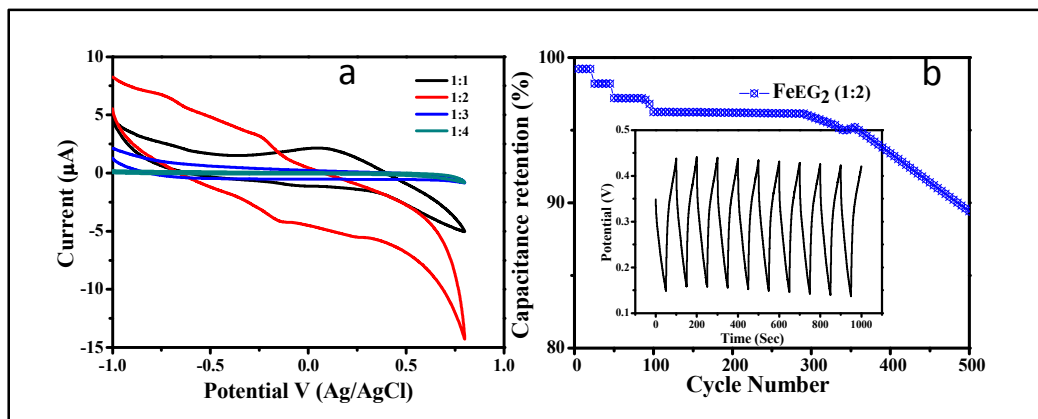


Figure 10. (a) Cyclic voltammograms of comparison plot for the sample synthesized at Fe: EG ratios = 1:1, 1:2, 1:3, 1:4 at different scan rates (5–100 mV/s) in 0.1 M Na₂SO₄ electrolyte in a three-electrode electrochemical cell (b) Typical charge–discharge plots for Fe:EG (1:2) samples at current density 5 mA g⁻¹ (c) CV of sample Fe:EG (1:2) for 500 cycles.

Conclusions:

In conclusion, novel processes for the formation of α -Fe₂O₃ phase have been established by a facile solvent mediated precipitation routes. The effect of synthetic parameters on the morphology, structure of the product, electrochemical properties and gas sensing behavior were also studied. Through concentration, reaction time and solvent-dependent experiments under simple solution route, it was definitely demonstrated that the morphology evolution of the α -Fe₂O₃ nanocrystals was controlled by facet growth species in the reaction. The facets with high surface energy tended to be formed in the reaction solution of high concentration EG, while the relatively more stable facets, such as (012) or (001), were favored in the reaction solution of lower concentration of EG while (012) plane oriented hematite nano flowers has been achieved by the assembly of pseudo cubes with (012) facets and a secondary growth process. The possible formation mechanism was proposed. By simply varying the concentration of EG, α -Fe₂O₃ microstructures with different porosities and shapes can be readily obtained. The band gap values for our hematite particles are smaller as compared to the values reported for the direct band gap of many nano particulate hematite and have increasing trend with increase in Fe:EG ratio. The ultra-high pseudo capacitance value is of 450F/g

for the sample obtained at Fe:EG 1:2 is related to high surface area self-assembled structured of the samples.

ASSOCIATED CONTENT

Supporting Information. “This material is available free of charge via the Internet at <http://pubs.acs.org>.”

AUTHOR INFORMATION

Corresponding Author

Mamata Mohapatra*, *Hydro & Electrometallurgy Department, CSIR- Institute of Minerals and Materials Technology, Bhubaneswar- 751 013, Odisha, India.*

mamatamohapatra76@gmail.com, mamatamohapatra@yahoo.com

ACKNOWLEDGMENT

The authors are very much thankful to Prof. B. K. Mishra, Director, CSIR-IMMT, Bhubaneswar, for his kind permission and encouragement for doing this study. Authors are very much thankful to Dr. Bikash Ku Jena, Scientist CSIR-IMMT for his kind permission to access the electrochemical station. We are also thankful to the respective reviewer, who guides us for indexing SAED planes. Authors are thankful to Ajit Ku Dash, CSIR-IMMT for helping us in calculating crystal planes using GATAN software. The first author is very much grateful to DST-India (Inspire Division) Financial support.

REFERENCES

- (1) Chaudhari, N. K.; Kim, H. C.; Kim, C. S.; Park, J.; Yu, J.-S. *Cryst Eng Comm.* **2012**, 14, 2024.
- (2) He, S.; Wang, G. S.; Wang, J. W.; Wei, Y. Z.; Wu, Y.; Guo, L.; Cao, M. S. *Chem Plus Chem.* **2013**, 78, 875–883.

- (3) Ouyang, J.; Pei, J.; Kuang, Q.; Xie, Z.; Zheng, L. *ACS Appl. Mater. Interfaces*, **2014**, *6*, 12505–12514.
- (4) Barik, R.; Tripathy, S. K.; Mohapatra, M. *Journal of Materials Science*. **2014**, *49*, 5345–5354.
- (5) Agarwala, S.; Lim, Z. H.; Nicholson, E.; Ho, G. W. *Nanoscale* **2012**, *4*, 194–205.
- (6) Wu, W.; Hao, R.; Liu, F.; Su, X.; Hou, Y. *J. Mater. Chem. A* **2013**, *1*, 6888–6894.
- (7) Zhou, X.; Lan, J.; Liu, G.; Deng, K.; Yang, Y.; Nie, G.; Yu, J.; Zhi, L. *Angew. Chem., Int. Ed.* **2012**, *51*, 178–182.
- (8) Xu, B.; Huang, B.; Cheng, H.; Wang, Z.; Qin, X.; Zhang, X.; Dai, Y. *Chem. Commun.* **2012**, *48*, 6529–6531.
- (9) Cheng, X.-L.; Jiang, J.-S.; Hu, M.; Mao, G.-Y.; Bu, F.-X.; Lin, C.-C.; Zeng, Y.; Zhang, Q.-H. *Cryst Eng Comm.* **2012**, *14*, 7701–7708.
- (10) Cao, C.-Y.; Qu, J.; Yan, W.-S.; Zhu, J.-F.; Wu, Z.-Y.; Song, W.-G. *Langmuir* **2012**, *28*, 4573–4579.
- (11) Cha, H. G.; Kang, M. J.; Hwang, I. C.; Kim, H.; Yoon, K. B.; Kang, Y. S. *Chem. Commun.* **2015**, *51*, 6407–6410.
- (12) Chen, J. S.; Zhu, T.; Yang, X. H.; Yang, H. G.; Lou, X. W. *J. Am. Chem. Soc.* **2010**, *132*, 13162–13164.
- (13) Duan, X.; Mei, L.; Ma, J.; Li, Q.; Wang, T.; Zheng, W. *Chem. Commun.* **2012**, *48*, 12204–12206.
- (14) Sethuraman, B.; Purushothaman, K. K.; Muralidharan, G. *RSC Adv.* **2014**, *4*, 4631–4637.
- (15) Wang, D.; Li, Y.; Wang, Q.; Wang, T. *J Solid State Electrochem.* **2012**, *16*, 2095–2102.
- (16) Zhu, M.; Wang, Y.; Meng, D.; Qin, X.; Diao, G. *J. Phys. Chem. C* **2012**, *116*, 16276–16285.
- (17) Liu, J. Lee, E.; Kim, Y. T.; Kwon, Y. U. *Nanoscale* **2014**, *6*, 10643–10649.
- (18) Cai, J.; Chen, S.; Hu, J.; Wang, Z.; Ma, Y.; Qi, L. *Cryst Eng Comm.* **2013**, *15*, 6284–6288.
- (19) Fu, L.; Yu, H.; Li, Y.; Zhang, C.; Wang, X.; Shao, Z.; Yi, B. *Phys. Chem. Chem. Phys.* **2014**, *16*, 4284–4290.
- (20) Zhong, L. S.; Hu, J. S.; Liang, H. P.; Cao, A. M.; Song, W. G.; Wan, L. J. *Adv. Mater.* **2006**, *18*, 2426–2431.

- (21) Zheng, L. R.; Zhen, Z. Y.; Xia, H. R.; Jie, Z. Y.; Ping, Z. H. *Sci. China Phys. Mech. Astron.* **2011**, 54, 942-947.
- (22) Shivakumara, S. T.; Penki, R.; Munichandraiah, N. *J. Solid State Electrochem.* **2014**, 18, 1057–1066.
- (23) LaTempa, T. J.; Feng, X.; Paulose, M.; Grimes, C. A. *J. Phys. Chem. C* **2009**, 113, 16293–16298.
- (24) Wu, Z.; Yu, K.; Zhang, S.; Xie, Y. *J. Phys. Chem. C* **2008**, 112, 11307–11313.
- (25) Islama, M. S.; Kurawakia, J.; Kusumoto, Y.; Abdulla-Al-Mamun, M.; Bin Mukhlish, M. Z. *J. Sci. Res.* **2012**, 4, 99-107.
- (26) Cao, S. W.; Zhu, Y. J. *J. Phys. Chem. C* **2008**, 112, 6253-6257.
- (27) Zhou, X.; Zhao, G.; Liu, Y. *Mater. Lett.* **2013**, 95, 33–36.
- (28) Cao, H.; Wang, G.; Zhang, L.; Liang, Y.; Zhang, S.; Zhang, X. *Chem. Phys. Chem.* **2006**, 7, 1897 -1901.
- (29) Liang, H.; Chen, W.; Jiang, X.; Xu, X.; Xu, B.; Wang, Z. *J. Mater. Chem. A* **2014**, 2, 4340-4346.
- (30) Zhao, J.; Yang, P.; Chen, H. S.; Li, J.; Che, Q.; Zhua, Y.; Shia, R. *J. Mater. Chem. C* **2015**, 3, 2539–2547.
- (31) He, S.; Wang, G. S.; Wang, J. W.; Wei, Y. Z.; Wu, Y.; Guo, L.; Cao, M. S. *Chem. Plus Chem.* **2013**, 78, 875–883.
- (32) Guo, H.; Barnard, A. S. *J. Mater. Chem.* **2011**, 21, 11566-11577.
- (33) Liang, H.; Jiang, X.; Qi, Z.; Chen, W.; Wu, Z.; Xu, B.; Wang, Z.; Mic, J.; Lia, Q. *Nanoscale* **2014**, 6, 7199–7203.
- (34) Chen, L.; Yang, X.; Chen, J.; Liu, J.; Wu, H.; Zhan, H.; Liang, C.; Wu, M. *Inorg. Chem.* **2010**, 49, 8411–8420.
- (35) Barr' on, V.; Torrent, J. *J. Colloid Interface Sci.* **1996**, 177,407-410.
- (36) Huang, X. *J. Colloid Interface Sci.* **2004**, 271, 296-307.
- (37) Li, D.; Nielsen, M. H.; Lee, J. R. I.; Frandsen, C.; Banfield, J. F.; Yoreo, J. J. D. *Science* **2012**, 336, 1014–1018.
- (38) Niederberger, M.; Colfen, H. *Phys. Chem. Chem. Phys.* **2006**, 8, 3271–3287.

- (39) Wu, C. Z.; Yin, P.; Zhu, X.; Yang, C. Z. O.; Xie, Y. *J. Phys. Chem. B* **2006**, 110, 17806–17812.
- (40) Fang, X. L.; Chen, C.; Jin, M. S.; Kuang, Q.; Xie, Z. X.; Xie, S. Y.; Huang, R. B.; Zheng, L. S. *J. Mater. Chem.* **2009**, 19, 6154–6160.
- (41) Zheng, Y. H.; Cheng, Y.; Wang, Y. S.; Bao, F.; Zhou, L. H.; Wei, X. F.; Zhang, Y. Y.; Zheng, Q. *J. Phys. Chem. B* **2006**, 110, 3093–3097.
- (42) Nasibulin, A. G.; Rackauskas, S.; Jiang, H.; Tian, Y.; Mudimela, P. R.; Shandakov, S. D.; Nasibulina, L. I.; Sainio, J.; Kauppinen, E. I. *Nano Res.* **2009**, 2, 373–379.
- (43) Zhong, J. U.; Cao, C.; Liu, Y.; Li, Y.; Khan, W. S. *Chem. Commun.* **2008**, 46, 3869–3871.
- (44) Dong, Q.; Kumada, N.; Yonesaki, Y.; Takei, T.; Kinomura, N.; Wang, D.; *J. Mater. Sci.* **2010**, 45, 5685–5691.
- (45) Li, L.; Chu, Y.; Y. Liu and L. Dong, *J. Phys. Chem. C* **2007**, 111, 2123–2127.
- (46) Gregg, S. J.; Sing, K. S. W. *Adsorption, Surface Area and Porosity; Academic Press: London*, **1982**.
- (47) Braga, T. P.; Pinheiro, A. N.; Herrera, W. T.; Xing, Y. T.; Saitovitch, E. B.; Valentini, A. *J Mater. Sci.* **2011**, 46, 766–773.
- (48) Cherian, C. T.; Sundaramurthy, J.; Kalaivani, Ragupathy, M. P.; Suresh Kumar, P.; Thavasi, V.; Reddy, M. V.; Sow, C. H.; Mhaisalkar, S. G.; Ramakrishna, S.; Chowdari, B. V. R. *J. Mater. Chem.* **2012**, 22, 12198–12204.
- (49) Cao, R.; Chen, X.; Shen, W.; Long, Z. *Mater. Lett.* **2011**, 65, 3298–3300.
- (50) Zhang, Z.; Takahashi, T.; Hossain, M. F. *Mater. Lett.* **2010**, 64, 435–438.
- (51) Lian, J. B.; Duan, X. C.; Ma, J. M.; Peng, P.; Kim, T. I.; Zheng, W. J. *ACS Nano* **2009**, 3, 3749–3761.
- (52) Mitra, S.; Das, S.; Mandal, K.; Chaudhuri, S. *Nanotechnology* **2007**, 18, 275608, 9pp.
- (53) Cherepy, N. J.; Liston, D. B.; Lovejoy, J. A.; Deng, H.; Zhang, J. Z. *J. Phys. Chem. B* **1998**, 102, 770–776.

- (54) Chatterjee, S.; Sarkar, S.; Bhattacharyya, S. N. *J. Photochem. Photobiol. A* **1993**, 72, 183–187.
- (55) Fan, H. M.; You, G. J.; Li, Y.; Zheng, Z.; Tan, H. R.; Shen, Z. X.; Tang, S. H.; Feng, Y. P. *J. Phys. Chem. C* **2009**, 113, 9928–9935.
- (56) Lu, L.; Li, L.; Wang, X.; Li, G. *J. Phys. Chem. B*, **2005**, 109, 17151–17156.
- (57) Woodward, P. M.; Mizoguchi, H.; Y. I. Kim and M. W. Stoltzfus and J. L. G. Fierro, CRC Press/Taylor & Francis Group, Boca Raton, FL, **2006**, 783.
- (58) Chernyshova, I. V.; Ponnurangam, S.; Somasundaran, P. *Phys. Chem. Chem. Phys.* **2010**, 12, 14045–14056.
- (59) Nuli, Y.; Zhang, P.; Guo, Z.; Liu, H.; *J. Electrochem. Soc.* **2008**, 155, A196–A200.
- (60) Wang, H.; Xua, Z.; Yia, H.; Weib, H.; Guom, Z.; Wanga, X. *Nano Energy* **2014**, 7, 86–96.
- (61) Veluria, P. S.; Mitra, S. *RSC Adv.* **2013**, 3, 15132–15138.
- (62) Shou, Q.; Cheng, J.; Zhang, L.; Nelson, B. J.; Zhang, X. *J. Solid State Chem.* **2012**, 185, 191–197.
- (63) Li, Z. C.; Guan, M. Y.; Lou, Z. S.; Shang, T. M. *Micro & Nano Letters* **2012**, 7, 33–36.
- (64) Urbaniak, J.; Skowroński, J. M.; Olejnik, B. *J. Solid State Electrochem.* **2010**, 14, 1629–1635.
- (65) Jayalakshmi, M.; Balasubramanian, K. *Int. J. Electrochem. Sci.* **2009**, 4, 878 – 886.
- (66) Low, Q. X.; Ho, G.W. *Nano Energy* **2014**, 5, 28–35.
- (67) Wang, D.; Wang, Q.; Wang, T. *Nanotechnology* **2011**, 22, 135604–135615.
- (68) Xie, K.; Li, J.; Lai, Y.; Lu, W.; Zhang, Z.; Liu, Y; Zhou, L.; Huang, H. *Electrochem Commun.* **2011**, 13, 657–660.
- (69) Zhu, M.; Wang, Y.; Meng, D.; Qin, X.; Diao, G. *J. Phys. Chem. C* **2012**, 116, 16276–16285.